Bleier, N.; Mosler, J.:

A hybrid variationally consistent homogenization approach based on Ritzs method

In: International Journal for Numerical Methods in Engineering (2013) Wiley

DOI: 10.1002/nme.4465

A hybrid variationally consistent homogenization approach based on Ritz's method

N. Bleier

Institute of Mechanics
Ruhr University Bochum
D-44780 Bochum, Germany

J. Mosler

Institute of Mechanics
TU Dortmund
D-44227 Dortmund, Germany
E-Mail: joern.mosler@tu-dortmund.de

SUMMARY

Multiscale approaches based on homogenization theory provide a suitable framework to incorporate information associated with a small scale (microscale) into the considered large scale (macroscopic) problem. In this connection, the present paper proposes a novel computationally efficient hybrid homogenization method. Its backbone is a variationally consistent FE^2 approach in which every aspect is governed by energy minimization. Particularly, scale bridging is realized by the canonical principle of energy equivalence. Since a direct implementation of the aforementioned variationally consistent FE^2 approach is numerically extensive, an efficient approximation based on Ritz's method is advocated. By doing so, the material parameters defining an effective macroscopic material model capturing the underlying microstructure can be efficiently computed. Furthermore, the variational scale bridging principle provides some guidance to choose a suitable family of macroscopic material models. Comparisons between the results predicted by the novel hybrid homogenization method and full field finite element simulations show that the novel method is indeed very promising for multiscale analyses.

1 Introduction

The macroscopic mechanical response of materials is generally defined by the underlying microstructure which, in turn, is related to the atomistic and electron structure. Although a direct phenomenological description at the macroscale is possible in principle, such a procedure shows several problems. On the one hand, it is at best a projection of some microscale constitutive model. Consequently and common to all projection techniques, significant information is lost and, thus, important features cannot be captured. On the other hand, a direct macroscopic approach often leads to very complicated equations involving higher-order tensors which cannot be interpreted in a straightforward manner from a physics point of view, cf. [1]. A full field simulation reflecting all features of the smallest scale involved is not an alternative either, since the size of the resulting set of equations associated with the considered macroscopic engineering problem is usually too large, resulting in prohibitive numerical costs.

As a compromise between the aforementioned limiting cases, multiscale approaches based on homogenization concepts represent a promising avenue to assert the macroscopic behavior of a system showing a complex microstructure, cf. [2, 3]. Comprehensive overviews concerning numerical implementations of multiscale approaches can be found in [4–7] and references cited therein. Common to most homogenization methods is that a representative volume element (RVE) is considered within such approaches. This element is subjected to some boundary conditions reflecting the macroscopic loading. Subsequently, the boundary value problem (bvp) characterizing the RVE's mechanical response is solved and the macroscopic response (stress or strain) is computed by some averaging technique, cf. [2, 3].

Finding the solution of the bvp associated with the RVE certainly is computationally extensive. In the case of linear problems, the deformation within the RVE can fortunately be determined analytically. In this connection, the eigenstrain method going back to Eshelby is noteworthy, see [8, 9]. This mean field theory represents the cornerstone of most analytical homogenization methods. For instance, extensions of Eshelby's ideas led to the well-known self-consistent method proposed by Budiansky and Hill, cf. [10, 11] as well as to the Mori-Tanaka method, see [12]. Other analytical homogenization approaches as well as the classical bounds of Voigt/Taylor- (also known as the Cauchy-Born hypothesis in the context of atomistic models) or of Sachs/Reuss-type can be found in the excellent overviews [2, 3] and references cited therein. It bears emphasis that the classification as analytical method does not imply that computations are completely avoided. A representative example is given by the so-called viscoplastic self-consistent (VPSC) model [13].

Although the aforementioned analytical homogenization concepts are very appealing from a practical point of view, since numerically extensive computations are not required, their range of application is relatively narrow. This is mostly due to the underlying assumptions. For instance, the frequently considered superposition principle is only valid for linear problems, cf. [3]. By way of contrast computational homogenization schemes do not show this constraint. Among those, the so-called FE^2 approach originally proposed in [14, 15] is probably the most frequently applied one. For a recent and comprehensive overview, the interested reader is referred to [6]. In contrast to analytical methods, the bvp problem governing the mechanical response of the microscale is numerically solved by a finite element approximation within FE^2 approaches. On the one hand, that leads to a very general framework which can be applied to almost any material model including those showing a highly nonlinear stress strain response and dissipation. More explicitly, almost no restrictions associated with the constitutive model at the microstructure exist. On the other hand, this broad range of application comes along with a high computational complexity. Particularly, the computation of the algorithmic tangent at the macroscale necessary for an asymptotically quadratic convergence slows down the algorithm. For this reason, large scale FE^2 approaches are often not practical, although a parallel implementation is relatively straightforward.

As a compromise between numerical efficiency (closed-form solutions of analytical homogenization methods) and a broad range of applications (numerical homogenization approaches such as the FE^2 method), hybrid methods are promising. One such method is the non-uniform transformation field analysis (NTFA) originally proposed in [16]. In contrast to classical analytical homogenization concepts, the key idea within the NTFA is the approximation of the most relevant deformation modes at the microscale. Focusing on plastic deformation, the plastic strain field was thus considered in [16] and decomposed into time-constant modes and time-varying amplitudes the rates of which are, in turn, computed from suitable evolution equations. Consequently and in line with the classical finite element method, the approximation of an infinite-dimensional field by a suitable finite-dimensional approximation is one of the key ideas of the NTFA.

The hybrid method which will be discussed in the present paper is also based on a finite-dimensional approximation. The starting point is a variationally consistent FE^2 approach [5, 6], the backbone of which is a variationally consistent description of the constitutive models at the microscale, cf. [5, 17–20, 20–22]. Without going into too much detail, every single aspect is naturally driven by energy minimization within the resulting approach. For instance, energy stability of the RVE naturally yields the updated state variables as well as the fluctuation field at the microscale. Furthermore, this minimization naturally leads to an effective macroscopic potential which defines the macroscopic stresses. Recently, the aforementioned variationally consistent FE^2 approach has also been employed in order to derive an efficient mean-field-based homogenization concept, cf. [23]. However, besides the underlying variational homogenization approach, the method discussed in the present paper differs significantly from that proposed in [23]. For instance, almost no assumptions regarding the constitutive response are required. By way of contrast, the scheme elaborated in [23] relies heavily on the structure of von Mises plasticity theory - although the approach in [23] could in principle also be applied to other constitutive models.

Although the scheme [5, 6] is mathematically and from a physics point of view very elegant, a straightforward implementation shows the same numerical complexity as standard FE^2 approaches. For this reason, a novel variationally consistent approximation is proposed in the present paper. More precisely and analogously to Ritz's method, the key idea is a finite-dimensional approximation of the infinite-dimensional space of effective macroscopic material models. With this approximation, the material parameters defining the considered effective macroscopic material follow naturally from the underlying minimization principle. Thus, and in contrast to classical FE^2 approaches, a closed-form approximation for the effective material model is obtained by the principle of energy equivalence. The choice of the finite-dimensional approximation certainly influences the resulting model. However, it will be shown that the underlying variational principle provides some guidance to choose a proper approximation. This will be confirmed by comparisons between the results predicted by the novel hybrid homogenization method and those related to a full field finite element simulation.

Certainly, the idea to identify material parameters of a macroscopic phenomenological model from numerical analyses of representative volume elements is not new, but can be found, e.g., in [24–26]. While in [24, 25] the model parameters of macroscopic yield functions have been determined by a standard least square fit in which the predictions of a macroscopic model were compared to those of a microscopic model (RVE), the parameters of an interface model were identified in [26] by minimizing the error between the averaged stresses (homogenized) resulting from a representative volume element (Gurson model) and those associated with a macroscopic cohesive zone model. The same least-squares fitting approach is also often applied, if the parameters of a macroscopic phenomenological model are to be determined based on experimentally measured data, cf. [27, 28], i.e. , conceptually, it is not important, if the material response

is known due to real or virtual experiments (representative volume elements). In any case, the crucial point is the definition of the objective function to be minimized (the error). Usually, an ad-hoc heuristic approach is followed. By way of contrast, the novel approach based on energy minimization, which will be discussed in this paper, derives consistently from a variational FE^2 approach. In this respect, it bridges the gap between consistent FE^2 methods and classical ad-hoc material parameter identification procedures, i.e., an ad-hoc definition of an objective function is not required.

This paper is set up as follows: Section 2 deals with finite strain plasticity theory and its variationally consistent reformulation. Within the resulting model, all unknown variables such as the plastic strains follow naturally from minimizing the stress power. Subsequently, an overview about computational homogenization concepts is given in Section 3. In this connection, focus is on variationally consistent FE^2 approaches based on the principle of energy equivalence. The aforementioned efficient approximation based on Ritz's method is elaborated in Section 4. It represents the main novel contribution of the present paper. The applicability as well as the performance of the novel homogenization concept are finally analyzed in Section 5.

2 A variational formulation of finite strain plasticity theory

The hybrid homogenization method to be discussed in the present paper represents a general framework which can be applied to a broad range of different constitutive models. A variational structure is the only requirement for this method. More precisely, the underlying constitutive models have to be based on energy minimization. However, according to [5, 17–20, 22], this constraint is only relatively weak and thus fulfilled for most of the relevant material models. For instance, all models falling into the class of *standard dissipative solids* in the sense of Halphen & Nguyen [29] are covered. Recently, it was shown that even models based on non-associative flow rules or evolution equations can sometimes be rewritten in a variationally consistent form, cf. [21, 30]. For that purpose, a generalized principle of maximum dissipation related to *generalized standard materials* was considered in [21, 30], see also [31, 32]. Other examples for constitutive models based on energy minimization include, among others, those for deformation-induced twinning [33, 34], thermomechanically coupled phenomena [35, 36], the evolution of microstructures [37–39] or gradient-enhanced continua [40, 41].

According to the cited papers and references therein, the existence of a minimization principle is not a very strict requirement. For this reason, the paper could be written without specifying the precise form of the functional to be minimized. However, some important aspects concerning the numerical implementation could not be discussed in detail in this case. For this reason, the authors have chosen a well-known constitutive model as a prototype which shows a variational structure. To be more precise, finite strain plasticity theory shall be considered in the following.

2.1 Fundamentals

The fundamentals of plasticity theory at finite strains as well as the used notations are briefly introduced here. A summary of the most important equations is given in Tab. 1. According to that table, the yield function, the flow rule and the evolution equations are defined with respect to the intermediate configuration. Hence, the principle of material frame indifference is automatically fulfilled. Furthermore, associative evolution equations and an associative flow rule are adopted for the sake of simplicity. However, and as shown in [21, 30], variational principles can even be derived for some models not obeying the classical normality rule. The only technical requirement for rate-independent models is the positive homogeneity of degree one of the equivalent stress measure (see Eq. (4)). This technical point will be discussed later.

2.2 A variational reformulation

In line with the previous subsection, the fundamentals associated with the variational structure of finite strain plasticity theory are given here in a nutshell. The most important aspects are summarized in Tab. 2. For the sake of completeness, the equivalence between the classical formulation of finite strain plasticity according to Tab. 1 and the variational reformulation presented in Tab. 2 is briefly discussed. For that purpose, energy minimization of the stress power $\mathcal{E}$ with respect to the plastic multiplier λ is

- Multiplicative decomposition of the deformation gradient $\boldsymbol{F}$ into the elastic part $\boldsymbol{F}^{\mathrm{e}}$ and the plastic part $\boldsymbol{F}^{\mathrm{p}}$, cf. [42, 43]

$$\boldsymbol{F} = \boldsymbol{F}^{\mathrm{e}} \cdot \boldsymbol{F}^{\mathrm{p}}, \quad \text{with} \quad \det \boldsymbol{F}^{\mathrm{e}} > 0 \quad \text{and} \quad \det \boldsymbol{F}^{\mathrm{p}} > 0 \tag{1}$$

- Additive decomposition of the Helmholtz energy Ψ

$$\Psi = \Psi^{\mathrm{e}}(\boldsymbol{C}^{\mathrm{e}}) + \Psi^{\mathrm{p}}(\boldsymbol{\alpha}), \quad \text{with} \quad \boldsymbol{C}^{\mathrm{e}} := \boldsymbol{F}^{\mathrm{e}\mathrm{T}} \cdot \boldsymbol{F}^{\mathrm{e}} \tag{2}$$

  Here, $\boldsymbol{\alpha} \in \mathbb{R}^n$ is a set of internal strain-like variables associated with hardening.

- Stress tensors following from the second-law of thermodynamics

$$\boldsymbol{P} = \partial_{\boldsymbol{F}} \Psi, \qquad \boldsymbol{\Sigma} = 2\, \boldsymbol{C}^{\mathrm{e}} \cdot \partial_{\boldsymbol{C}^{\mathrm{e}}} \Psi \tag{3}$$

  In Eq. (3), $\boldsymbol{P}$ denotes the Kirchhoff stresses and $\boldsymbol{\Sigma}$ are the Mandel stresses with respect to the intermediated configuration.

- Space of admissible stresses $\mathbb{S}_{\boldsymbol{\Sigma}}$ defined by a convex yield function ϕ which is based on a positively homogeneous function Σ^{eq} of degree one

$$\mathbb{S}_{\boldsymbol{\Sigma}} = \left\{ (\boldsymbol{\Sigma}, \boldsymbol{Q}) \in \mathbb{R}^{9+n} \;\middle|\; \phi(\boldsymbol{\Sigma}, \boldsymbol{Q}) = \Sigma^{\mathrm{eq}}(\boldsymbol{\Sigma}, \boldsymbol{Q}) - Q_0 \leq 0 \right\} \tag{4}$$

  where $\boldsymbol{Q} := -\partial_{\boldsymbol{\alpha}} \Psi^{\mathrm{p}} \in \mathbb{R}^n$ is the stress-like internal variable conjugate to $\boldsymbol{\alpha}$.

- Associative flow rule and evolution equations

$$\boldsymbol{L}^{\mathrm{p}} = \dot{\boldsymbol{F}}^{\mathrm{p}} \cdot \boldsymbol{F}^{\mathrm{p}\,-1} = \lambda\, \partial_{\boldsymbol{\Sigma}} \phi, \qquad \dot{\boldsymbol{\alpha}} = \lambda\, \partial_{\boldsymbol{Q}} \phi \tag{5}$$

  Here, λ denotes the plastic multiplier and the superposed dot represents the material time derivative.

- Karush-Kuhn-Tucker optimality conditions

$$\lambda \geq 0, \quad \phi \leq 0, \quad \lambda\, \phi = 0 \tag{6}$$

- Dissipation inequality and its reduced form

$$\mathcal{D} = \boldsymbol{P} : \dot{\boldsymbol{F}} - \dot{\Psi} = \boldsymbol{\Sigma} : \boldsymbol{L}^{\mathrm{p}} - \dot{\Psi}^{\mathrm{p}} = \lambda\, Q_0 \geq 0 \tag{7}$$

Table 1: Fundamental equations defining associative rate-independent plasticity theory at finite strains

- Stress power for admissible states

$$\mathcal{E}(\dot{\boldsymbol{F}}, \lambda, \boldsymbol{M}) = \boldsymbol{P} : \dot{\boldsymbol{F}} = \dot{\Psi} + \lambda\, Q_0 \tag{8}$$

  Here, $\boldsymbol{M} := \partial_{\boldsymbol{\Sigma}} \phi$ denotes the flow direction.

- Variational principle defining the rate of the internal variables (λ and $\boldsymbol{M}$)

$$(\lambda, \boldsymbol{M}) = \arg \inf_{\lambda, \boldsymbol{M}} \mathcal{E}|_{\dot{\boldsymbol{F}} = \boldsymbol{0}} \tag{9}$$

- Stresses derived from a pseudo potential

$$\boldsymbol{P} = \partial_{\dot{\boldsymbol{F}}} \mathcal{E}_{\mathrm{red}}, \qquad \mathcal{E}_{\mathrm{red}} := \inf_{\lambda, \boldsymbol{M}} \mathcal{E} \tag{10}$$

Table 2: The variational structure of associative finite strain plasticity, cf. [5, 17–20, 22]

analyzed. Computing the respective partial derivative of $\mathcal{E}$, the corresponding condition reads

$$\begin{aligned}\frac{\partial \mathcal{E}}{\partial \lambda} &= \frac{\partial \Psi^{\mathrm{e}}}{\partial \boldsymbol{F}^{\mathrm{e}}} : \frac{\partial \boldsymbol{F}^{\mathrm{e}}}{\partial \boldsymbol{F}^{\mathrm{p}}} : (\partial_{\boldsymbol{\Sigma}}\phi \cdot \boldsymbol{F}^{\mathrm{p}}) + \frac{\partial \Psi^{\mathrm{p}}}{\partial \boldsymbol{\alpha}} \cdot \partial_{\boldsymbol{Q}}\phi + Q_0 \\ &= -\boldsymbol{\Sigma} : \partial_{\boldsymbol{\Sigma}}\phi - \boldsymbol{Q} \cdot \partial_{\boldsymbol{Q}}\phi + Q_0 \\ &= -\phi \geq 0.\end{aligned} \tag{11}$$

Hence, energy minimization enforces admissible stress states, i.e. $\phi \leq 0$. Further details are omitted here, but can be found, e.g. in [5, 17–20, 22].

Although the minimization principle (9) is conceptually very simple, the nonlinear constraints resulting from the flow rule $\boldsymbol{M} = \partial_{\boldsymbol{\Sigma}}\phi$ require special care. One efficient approach which fulfills such constraints a priori was recently proposed in [20]. It is based on the concept of so-called *pseudo stresses*, denoted as $\tilde{\boldsymbol{\Sigma}}$ which are not necessarily identical to their real counterparts $\boldsymbol{\Sigma}$. However, they lead to the same flow direction, i.e., $\boldsymbol{M} = \partial_{\boldsymbol{\Sigma}}\phi|_{\boldsymbol{\Sigma}} = \partial_{\boldsymbol{\Sigma}}\phi|_{\tilde{\boldsymbol{\Sigma}}}$. Introducing these pseudo stresses, minimization principle (9) now reads

$$(\lambda, \tilde{\boldsymbol{\Sigma}}) = \arg \inf_{\lambda, \tilde{\boldsymbol{\Sigma}}} \mathcal{E}(\dot{\boldsymbol{F}}, \lambda, \tilde{\boldsymbol{\Sigma}})\big|_{\dot{\boldsymbol{F}}=\boldsymbol{0}}\,. \tag{12}$$

Further details can be found in [20, 22].

2.3 Numerical implementation

Based on variational principle (12) a numerical implementation can be developed in a natural way. For this purpose, a time interval $[t_n; t_{n+1}]$ is considered and the continuous problem (12) is transformed into its discrete counterpart

$$(\Delta\lambda, \tilde{\boldsymbol{\Sigma}}_{n+1}) = \arg \inf_{\Delta\lambda, \tilde{\boldsymbol{\Sigma}}_{n+1}} I_{\mathrm{inc}}|_{\boldsymbol{F}_{n+1}=\mathrm{const}} \tag{13}$$

with

$$I_{\mathrm{inc}}(\boldsymbol{F}_{n+1}, \Delta\lambda, \tilde{\boldsymbol{\Sigma}}_{n+1}) := \int_{t_n}^{t_{n+1}} \mathcal{E}\ \mathrm{d}t = \Psi_{n+1} - \Psi_n + \Delta\lambda\, Q_0, \quad \Delta\lambda := \int_{t_n}^{t_{n+1}} \lambda\ \mathrm{d}t. \tag{14}$$

The computation of Ψ_{n+1} requires the updated deformation gradient $\boldsymbol{F}^{\mathrm{p}}_{n+1}$ as well as the internal variables $\boldsymbol{\alpha}_{n+1}$. Regarding $\boldsymbol{F}^{\mathrm{p}}_{n+1} = \boldsymbol{F}^{\mathrm{p}}_{n+1}(\Delta\lambda, \tilde{\boldsymbol{\Sigma}}_{n+1})$, an implicit time integration based on the exponential map is employed, while the internal variables $\boldsymbol{\alpha}$ are integrated by means of a standard backward Euler integration. Once problem (13) has been solved, the update of the stresses is given by

$$\boldsymbol{P}_{n+1} = \frac{\partial I^{\mathrm{red}}_{\mathrm{inc}}}{\partial \boldsymbol{F}_{n+1}}, \qquad I^{\mathrm{red}}_{\mathrm{inc}} = \inf_{\Delta\lambda, \tilde{\boldsymbol{\Sigma}}_{n+1}} I_{\mathrm{inc}}|_{\boldsymbol{F}_{n+1}=\mathrm{const}}\,. \tag{15}$$

As mentioned in [22], a minimization of Eq. (14) by using the classical Newton-Raphson scheme can lead to numerical problems, since the Hessian of I_{inc} can be singular. This is strongly related to the positive homogeneity of the equivalent stress Σ^{eq} of degree one. In this case,

$$\boldsymbol{M}(\tilde{\boldsymbol{\Sigma}}) = \left.\frac{\partial \phi}{\partial \boldsymbol{\Sigma}}\right|_{\tilde{\boldsymbol{\Sigma}}} = \left.\frac{\partial \phi}{\partial \boldsymbol{\Sigma}}\right|_{c\,\tilde{\boldsymbol{\Sigma}}} = \boldsymbol{M}(c\,\tilde{\boldsymbol{\Sigma}}), \qquad \forall c \in \mathbb{R}^+. \tag{16}$$

In order to eliminate this non-uniqueness, the tensor $\tilde{\boldsymbol{\Sigma}}$ can be normalized. In [22] that was implemented by a spectral decomposition of the type

$$\tilde{\boldsymbol{\Sigma}} := \sum_{k=1}^{3} \tilde{\Sigma}_k(\psi, \rho)\ \boldsymbol{B}_k \tag{17}$$

with the eigenvalues

$$\tilde{\Sigma}_1 = \sin\psi\cos\rho, \quad \tilde{\Sigma}_2 = \sin\psi\sin\rho, \quad \tilde{\Sigma}_3 = \cos\psi \tag{18}$$

depending on the angles ρ and ψ. For a symmetrical flow rule, the basis $\boldsymbol{B}_k$ is also symmetric and can be defined by three Euler angles, whereas for an unsymmetrical flow rule, six angles are required. Further details on the implementation of variational constitutive updates are provided in [22].

3 Computational homogenization methods based on energy minimization

Purely macroscopic phenomenological models such as those discussed in the previous section are sometimes not sufficient to capture all relevant features associated with the microscale. Efficient approaches allowing the incorporation of such features are provided by computational homogenization methods. In the present section, focus is on a special class of these methods – the so-called FE^2 approaches, cf. [14, 15]. For a recent and comprehensive overview, the interested reader is referred to [6]. In contrast to the most frequently applied FE^2 implementations, a variational framework in line with [6] is considered here. While the first part of the present section gives a concise state-of-the-art review concerning the fundamentals of FE^2 approaches with focus on variationally consistent formulations, numerical aspects are discussed at the end.

3.1 Fundamentals

In the following, a representative volume element $\mathcal{B}$ (RVE) consisting of the solid phase Ω and holes $\mathcal{H}$ is considered, i.e. $\mathcal{B} = \Omega \cup \mathcal{H}$. Variables describing the local state of constituents belonging to Ω (the microscale) are written in standard notation, e.g., $\boldsymbol{F}$ is the deformation gradient. In contrast, variables related to the average response of the RVE (macroscale) are denoted by overlined letters, e.g., $\bar{\boldsymbol{F}}$ is the macroscopic deformation gradient.

3.1.1 Kinematics

One cornerstone of multiscale concepts in general is the homogenization assumption (also known as prolongation assumption). In this connection and in line with [6] and others, the deformation gradient at the microscale is additively decomposed into that at the macroscale and a superposed fluctuation field denoted as $\boldsymbol{w}$, i.e.,

$$\boldsymbol{F} = \bar{\boldsymbol{F}} + \mathrm{GRAD}\boldsymbol{w}. \tag{19}$$

Accordingly, the deformation within the RVE is defined by

$$\boldsymbol{\varphi} = \bar{\boldsymbol{F}} \cdot \boldsymbol{X} + \boldsymbol{w}. \tag{20}$$

Consequently, Eq. (19) represents a first-order approximation which is computationally efficient, but which cannot capture size-effects. For higher-order computational homogenization schemes, the interested reader is referred to [44] . Certainly, the deformation at the microscale and that at the macroscale are coupled. That implies a constraint on the fluctuation field $\boldsymbol{w}$. Following [45], the deformation at the macroscale is computed from surface data of the microscale according to

$$\bar{\boldsymbol{F}} = \frac{1}{|\mathcal{B}|} \int_{\partial\mathcal{B}} \boldsymbol{\varphi} \otimes \boldsymbol{N} \, \mathrm{d}A \tag{21}$$

where $\boldsymbol{N}$ is the referential outward normal vector of the RVE. As becomes evident, the macroscopic deformation gradient defined by Eq. (21) is the standard average deformation gradient $1/|\mathcal{B}| \int_{\mathcal{B}} \boldsymbol{F} \, \mathrm{d}V$, if the RVE contains neither holes nor discontinuities. Thus, Eq. (21) justifies the interpretation of $\bar{\boldsymbol{F}}$ as the macroscopic deformation gradient. By inserting Eq. (19) into Eq. (21), the fluctuation field has to fulfill the condition

$$\frac{1}{|\mathcal{B}|} \int_{\partial\mathcal{B}} \boldsymbol{w} \otimes \boldsymbol{N} \, \mathrm{d}A = \boldsymbol{0}. \tag{22}$$

Eq. (22) can be a priori enforced by different choices such as the classical Taylor assumption $\boldsymbol{w} = \boldsymbol{0}$ $\forall \boldsymbol{X} \in \mathcal{B}$ or homogeneous fluctuations at the boundary ($\boldsymbol{w} = \boldsymbol{0}$ $\forall \boldsymbol{X} \in \partial\mathcal{B}$). The softest response is obtained by homogeneous traction boundary conditions. The respective stress state can be interpreted as a Lagrange multiplier enforcing Eq. (22) in a weak form. Between the limiting cases of homogeneous fluctuations and stresses at the boundary of the RVE, periodic boundary conditions for $\boldsymbol{w}$ represent another admissible choice complying with Eq. (22). The different mechanical response as predicted by the different boundary conditions can be effectively estimated by using the variational structure of the underlying constitutive response (if such a structure exists). This will be shown in the following paragraph.

3.1.2 Macroscopic stresses

Dual to Eq. (21), the macroscopic stresses $\bar{\boldsymbol{P}}$ are often defined by

$$\bar{\boldsymbol{P}} := \frac{1}{|\mathcal{B}|} \int\limits_{\partial\mathcal{B}} \boldsymbol{t} \otimes \boldsymbol{N} \, \mathrm{d}A \tag{23}$$

where $\boldsymbol{t}$ is the traction vector at the boundary of the RVE (referential description). In the case of stress-free holes, this definition of $\bar{\boldsymbol{P}}$ complies with the average stresses of the microscale, i.e. $\bar{\boldsymbol{P}} = 1/|\mathcal{B}| \int_{\mathcal{B}} \boldsymbol{P} \, \mathrm{d}V$. Furthermore, the macroscopic variables $\bar{\boldsymbol{F}}$ and $\bar{\boldsymbol{P}}$ introduced by Eq. (21) and Eq. (23), together with the aforementioned boundary conditions at the RVE, fulfill the so-called Hill-Mandel-condition, cf. [46]

$$\bar{\boldsymbol{P}} : \dot{\bar{\boldsymbol{F}}} = \frac{1}{|\mathcal{B}|} \int\limits_{\mathcal{B}} \boldsymbol{P} : \dot{\boldsymbol{F}} \, \mathrm{d}V. \tag{24}$$

According to Eq. (24), the average stress power at the microscale equals the one at the macroscale. Consequently, by assuming constitutive models showing a variational structure such as those discussed in Section 2, Eq. (24) can be rewritten into the compact notation

$$\bar{\mathcal{E}} = \frac{1}{|\mathcal{B}|} \int\limits_{\mathcal{B}} \mathcal{E} \, \mathrm{d}V. \tag{25}$$

Since Eqs. (21) and (23) imply Eq. (24) (respectively Eq. (25)), one could alternatively define the macroscopic stresses implicitly. To be more precise, one could postulate Eqs. (21) and (25). This idea will be elaborated within the next paragraph. Concerning elasticity, such ideas go back to [47], whereas for inelastic solids the interested reader is referred to [5, 6]. However, it bears emphasis that, although the framework presented here is eventually equivalent to that previously advocated in [5, 6], the underlying motivation is different. In [5, 6], the analogous structure of standard dissipative materials and hyperelasticity was the key observation. By way of contrast, the dependence between Eqs. (21), (23) and (25) represents the starting point within the present paper.

Combining Eq. (12) and Eq. (19) and assuming further that plasticity at the microscale is governed by the variational framework discussed in Subsection 2.2, the stress power at the microscale is a function of the type

$$\mathcal{E} = \mathcal{E}(\dot{\bar{\boldsymbol{F}}}, \dot{\boldsymbol{w}}, \lambda, \tilde{\boldsymbol{\Sigma}}). \tag{26}$$

In this case and in line with Eq. (12), the plastic multiplier λ as well as the flow direction represented by the pseudo stresses $\tilde{\boldsymbol{\Sigma}}$ follow from the variational principle

$$(\lambda, \tilde{\boldsymbol{\Sigma}}) = \arg \inf_{\lambda, \tilde{\boldsymbol{\Sigma}}} \mathcal{E}(\dot{\bar{\boldsymbol{F}}}, \dot{\boldsymbol{w}}, \lambda, \tilde{\boldsymbol{\Sigma}}) \Big|_{\dot{\boldsymbol{w}}=\mathrm{const}, \dot{\bar{\boldsymbol{F}}}=\mathrm{const}} \tag{27}$$

which, in turn, implicitly introduces the reduced stress power

$$\mathcal{E}_{\mathrm{red}}(\dot{\bar{\boldsymbol{F}}}, \dot{\boldsymbol{w}}) = \inf_{\lambda, \tilde{\boldsymbol{\Sigma}}} \mathcal{E}(\dot{\bar{\boldsymbol{F}}}, \dot{\boldsymbol{w}}, \lambda, \tilde{\boldsymbol{\Sigma}}). \tag{28}$$

By way of contrast, the reduced stress power at the macroscale does not depend on the fluctuation field $\boldsymbol{w}$, i.e

$$\bar{\mathcal{E}}_{\mathrm{red}} = \bar{\mathcal{E}}_{\mathrm{red}}(\dot{\bar{\boldsymbol{F}}}). \tag{29}$$

Accordingly, by inserting Eq. (28) and Eq. (29) into the homogenization condition (25), it is evident that the boundary conditions associated with $\boldsymbol{w}$ alone are not sufficient for a scale transition. To be more explicit, the fluctuation field $\boldsymbol{w}$ has to be known everywhere – also in the interior of the body. Typically, the fluctuation field is computed such that equilibrium at the microscale is fulfilled. Ignoring body forces within the RVE, the respective condition therefore reads

$$DIV\, \boldsymbol{P} = \boldsymbol{0} \qquad \boldsymbol{w} \in \mathcal{W}. \tag{30}$$

Here, $\mathcal{W}$ denotes the space of admissible fluctuation fields and hence, this space depends on the assumed boundary conditions of the RVE. As shown, e.g. in [5, 6, 47] (see also the seminal work [45]), Eq. (30) can be rewritten into the variational form

$$\dot{\boldsymbol{w}} = \arg \inf_{\dot{\boldsymbol{w}}} \left\{ \frac{1}{|\mathcal{B}|} \int\limits_{\mathcal{B}} \mathcal{E}_{\mathrm{red}}(\dot{\bar{\boldsymbol{F}}}, \dot{\boldsymbol{w}}) \, \mathrm{d}V \right\} \Bigg|_{\dot{\bar{\boldsymbol{F}}}=\mathrm{const}, \boldsymbol{w} \in \mathcal{W}} . \tag{31}$$

The equivalence of Eq. (30) and Eq. (31) can be proved in straightforward manner. For instance, the necessary condition for minimizing the averaged microscopic stress power reads

$$\frac{1}{|\mathcal{B}|}\int_{\mathcal{B}} \boldsymbol{P} : \mathrm{GRAD}\delta\boldsymbol{w}\ \mathrm{d}V = 0 \qquad \forall \delta\boldsymbol{w} \in \mathcal{W}_0. \tag{32}$$

Here, the definition of the first Piola-Kirchhoff stresses at the microscale $\boldsymbol{P} = \partial_{\boldsymbol{F}}\mathcal{E}_{\mathrm{red}}$ has been used. Accordingly, minimization principle (31) implies the principle of virtual work which is known to be equivalent to the strong form of equilibrium (30). Further technical details concerning the boundary conditions or the case of homogeneous prescribed tractions at the RVE are not considered here, but can be found in [6].

Combining Eq. (25) and Eq. (31), the reduced stress power at the macroscale is defined as

$$\bar{\mathcal{E}}_{\mathrm{red}}(\dot{\bar{\boldsymbol{F}}}) := \inf_{\dot{\boldsymbol{w}}} \left\{ \frac{1}{|\mathcal{B}|}\int_{\mathcal{B}} \mathcal{E}_{\mathrm{red}}(\dot{\bar{\boldsymbol{F}}}, \dot{\boldsymbol{w}})\ \mathrm{d}V \right\}\Bigg|_{\dot{\bar{\boldsymbol{F}}}=\mathrm{const}, \boldsymbol{w}\in\mathcal{W}} . \tag{33}$$

Since the macroscopic stress power can alternatively be written as

$$\bar{\mathcal{E}}_{\mathrm{red}}(\dot{\bar{\boldsymbol{F}}}) = \bar{\boldsymbol{P}} : \dot{\bar{\boldsymbol{F}}}, \tag{34}$$

the macroscopic stresses are simply the partial derivative of the averaged microscopic stress power, i.e.

$$\bar{\boldsymbol{P}} = \frac{\partial}{\partial \dot{\bar{\boldsymbol{F}}}} \inf_{\dot{\boldsymbol{w}}} \left\{ \frac{1}{|\mathcal{B}|}\int_{\mathcal{B}} \mathcal{E}_{\mathrm{red}}(\dot{\bar{\boldsymbol{F}}}, \dot{\boldsymbol{w}})\ \mathrm{d}V \right\}\Bigg|_{\dot{\bar{\boldsymbol{F}}}=\mathrm{const},\, \boldsymbol{w}\in\mathcal{W}} . \tag{35}$$

Further details can be found in [6].

Remark 1 *Once more, it bears emphasis that the starting point of the discussed variational homogenization concept was the kinematical assumption (21) and the postulate of energy equivalence (25). The definition of the stresses (35) is implied by these assumptions. That is in contrast to classical homogenization theories in which a scale transition for the strains as well as for the stresses is usually postulated. Conceptually, the difference between classical computational homogenization and the discussed variational approach can be sketched as follows:*

	Assumptions		*Consequences*
traditional	*Kinematics* (21) *Stresses* (21) *Boundary conditions*	$\Rightarrow$	*Hill-Mandel condition* (24)
variational	*Kinematics* (21) *Hill-Mandel condition* (24) *Boundary conditions*	$\Rightarrow$	*Stresses* (21)

(36)

Clearly, both formulations are equivalent in the case of classical boundary conditions such as the periodic boundary conditions employed in the present paper. However, this equivalence is not fulfilled in general.

3.2 Numerical aspects

The goal of the numerical implementation is the computation of the macroscopic stresses $\bar{\boldsymbol{P}}$ at time t_{n+1} based on the prescribed macroscopic strains $\bar{\boldsymbol{F}}_{n+1}$. This problem is common to all displacement-driven finite element implementations.

3.2.1 Boundary conditions for the RVE

In the following, only periodic boundary conditions for the fluctuations $\boldsymbol{w}$ will be considered. As a special case they include homogeneous boundary fluctuations, i.e., with $\mathcal{W}_{\mathrm{hom}}$ denoting the respective space and $\mathcal{W}_{\mathrm{per}}$ representing the space of admissible displacement fluctuations which are periodic, $\mathcal{W}_{\mathrm{hom}} \subset \mathcal{W}_{\mathrm{per}}$. Consequently,

$$\bar{\mathcal{E}}^{\mathrm{per}}(\dot{\bar{\boldsymbol{F}}}) \quad \leq \quad \bar{\mathcal{E}}^{\mathrm{hom}}(\dot{\bar{\boldsymbol{F}}}) \quad \leq \quad \bar{\mathcal{E}}^{\mathrm{Taylor}}(\dot{\bar{\boldsymbol{F}}}) \qquad \forall \dot{\bar{\boldsymbol{F}}} \tag{37}$$

with

$$\bar{\mathcal{E}}^{\mathrm{per}}(\dot{\bar{\boldsymbol{F}}}) := \inf_{\dot{\boldsymbol{w}}\in\mathcal{W}_{\mathrm{per}}} \left\{ \frac{1}{|\mathcal{B}|}\int_{\mathcal{B}} \mathcal{E}_{\mathrm{red}}(\dot{\bar{\boldsymbol{F}}},\dot{\boldsymbol{w}})\,\mathrm{d}V \right\}, \tag{38}$$

$$\bar{\mathcal{E}}^{\mathrm{hom}}(\dot{\bar{\boldsymbol{F}}}) := \inf_{\dot{\boldsymbol{w}}\in\mathcal{W}_{\mathrm{hom}}} \left\{ \frac{1}{|\mathcal{B}|}\int_{\mathcal{B}} \mathcal{E}_{\mathrm{red}}(\dot{\bar{\boldsymbol{F}}},\dot{\boldsymbol{w}})\,\mathrm{d}V \right\}, \tag{39}$$

$$\bar{\mathcal{E}}^{\mathrm{Taylor}}(\dot{\bar{\boldsymbol{F}}}) := \left\{ \frac{1}{|\mathcal{B}|}\int_{\mathcal{B}} \mathcal{E}_{\mathrm{red}}(\dot{\bar{\boldsymbol{F}}},\dot{\boldsymbol{w}})\,\mathrm{d}V \right\}\Bigg|_{\dot{\boldsymbol{w}}=\boldsymbol{0}}. \tag{40}$$

According to Eq. (37), periodic boundary conditions lead to a softer mechanical response, because they are less restrictive ($\emptyset \subset \mathcal{W}_{\mathrm{hom}} \subset \mathcal{W}_{\mathrm{per}}$). Similarly, one can show that the softest response is provided by homogeneous traction conditions. For such boundary conditions, the implementation has to be modified significantly, cf. [6]. In practice, periodic boundary conditions bounded by the limiting cases of homogeneous fluctuations (or the even more restrictive Taylor assumption $\boldsymbol{w} = \boldsymbol{0}$) and homogeneous tractions have proven to yield usually the most realistic mechanical response, cf. [6]. For this reason, such boundary conditions will also be considered in the present paper.

3.2.2 Update of the macroscopic stresses

In this section, the computation of the macroscopic stresses $\bar{\boldsymbol{P}}$ at pseudo time t_{n+1} is briefly presented, see also [6]. In this connection, an underlying displacement-driven finite element formulation is assumed. Accordingly, the macroscopic deformation gradient at time t_{n+1} denoted as $\bar{\boldsymbol{F}}_{n+1}$ is known a priori. With this notation, the backward-Euler approximation of the microscopic stress power (see Eq. (14)) integrated over the time interval $[t_n; t_{n+1}]$ yields

$$I_{\mathrm{inc}} := \int_{t_n}^{t_{n+1}} \mathcal{E}\,\mathrm{d}t = \Psi_{n+1}(\bar{\boldsymbol{F}}_{n+1}, \boldsymbol{w}_{n+1}, \Delta\lambda, \tilde{\boldsymbol{\Sigma}}_{n+1}) - \Psi_n + \Delta\lambda\, Q_0. \tag{41}$$

Based on this incrementally defined energy, the respective macroscopic energy is introduced by the variational principle

$$\bar{I}_{\mathrm{inc}}(\bar{\boldsymbol{F}}_{n+1}) := \inf_{\boldsymbol{w}_{n+1}} \inf_{\Delta\lambda,\tilde{\boldsymbol{\Sigma}}_{n+1}} \left\{ \frac{1}{|\mathcal{B}|}\int_{\mathcal{B}} I_{\mathrm{inc}}(\bar{\boldsymbol{F}}_{n+1}, \boldsymbol{w}_{n+1}, \Delta\lambda, \tilde{\boldsymbol{\Sigma}}_{n+1})\,\mathrm{d}V \right\} \tag{42}$$

which, in turn, leads to the updated macroscopic stresses

$$\bar{\boldsymbol{P}}_{n+1} = \frac{\partial \bar{I}_{\mathrm{inc}}(\bar{\boldsymbol{F}}_{n+1})}{\partial \bar{\boldsymbol{F}}_{n+1}}. \tag{43}$$

It bears emphasis that the integrated plastic multiplier $\Delta\lambda$ and the pseudo stresses $\tilde{\boldsymbol{\Sigma}}$ in Eq. (42) have to be interpreted as fields, i.e., they can vary within the RVE.

In order to solve Eq. (42), the microscopic deformation $\boldsymbol{\varphi}$ is discretized by using finite elements. Thus,

$$\boldsymbol{\varphi}^e_{n+1} = \sum_{i=1}^{n} N_i \left(\bar{\boldsymbol{F}}_{n+1} \cdot \boldsymbol{X}^{(i)} + \boldsymbol{w}^{(\mathrm{i})}_{n+1} \right) \tag{44}$$

within a certain element e where N_i are the shape functions, $\boldsymbol{X}^{(i)}$ are the nodal coordinates (reference configuration) and $\boldsymbol{w}^{(\mathrm{i})}_{n+1}$ is the fluctuation field at node i. Since $\bar{\boldsymbol{F}}_{n+1}$ is constant within Eq. (42), $\Delta\boldsymbol{w}_{n+1} = \Delta\boldsymbol{\varphi}^e$ (here $\Delta(\bullet)$ represents the change of $(\bullet)$ in a finite time step at the microscale). As a result, periodic fluctuations can be equivalently enforced by constraining the change in the microscopic deformation field. This can clearly be implemented in a straightforward manner – at least, in the case of regular boundary triangulations, i.e., if the master and the slave side of the RVE show the same surface discretization.

According to Eq. (44), the microscopic deformation (respectively $\boldsymbol{w}$) is continuously approximated. This is necessary since it enters the energy through the deformation gradient. By way of contrast, the

increment of the internal variables characterized by $\Delta\lambda$ and $\tilde{\boldsymbol{\Sigma}}_{n+1}$ enter the energy directly. For this reason, they can conveniently be approximated locally. Consequently, Eq. (42) can be written as

$$I_{\text{inc}}(\bar{\boldsymbol{F}}_{n+1}) := \inf_{\boldsymbol{w}_{n+1}} \left\{ \frac{1}{|\mathcal{B}|} \int_{\mathcal{B}} \inf_{\Delta\lambda, \tilde{\boldsymbol{\Sigma}}_{n+1}} I_{\text{inc}}(\bar{\boldsymbol{F}}_{n+1}, \boldsymbol{w}_{n+1}, \Delta\lambda, \tilde{\boldsymbol{\Sigma}}_{n+1}) \, \mathrm{d}V \right\}. \tag{45}$$

In line with standard computational plasticity theory (see [48, 49]), Eq. (45) is solved in a staggered fashion. More explicitly, the fluctuation field $\boldsymbol{w}_{n+1}$ is computed first by fixing the internal variables, i.e.

$$\boldsymbol{w}_{n+1} = \arg \inf_{\boldsymbol{w}_{n+1}} \left\{ \frac{1}{|\mathcal{B}|} \int_{\mathcal{B}} I_{\text{inc}}(\bar{\boldsymbol{F}}_{n+1}, \boldsymbol{w}_{n+1}, \Delta\lambda, \tilde{\boldsymbol{\Sigma}}_{n+1}) \, \mathrm{d}V \right\} \Bigg|_{\bar{\boldsymbol{F}}_{n+1}, \Delta\lambda, \tilde{\boldsymbol{\Sigma}} = \text{const}}. \tag{46}$$

This can be realized by classical optimization algorithms (see [50, 51]) or by solving the corresponding necessary condition

$$\left\{ \frac{1}{|\mathcal{B}|} \int_{\mathcal{B}} \boldsymbol{P} : \text{GRAD}\delta\boldsymbol{w} \, \mathrm{d}V \right\} \Bigg|_{\bar{\boldsymbol{F}}_{n+1}, \Delta\lambda, \tilde{\boldsymbol{\Sigma}} = \text{const}} = 0 \qquad \forall \delta\boldsymbol{w} \in \mathcal{W}_0 \tag{47}$$

being equivalent to the principal of virtual work. Using the solution $\boldsymbol{w}_{n+1}$, the internal variables are updated within the RVE (typically at all integration points). They follow from the spatially local variational principle

$$(\Delta\lambda, \tilde{\boldsymbol{\Sigma}}_{n+1}) = \arg \inf_{\Delta\lambda, \tilde{\boldsymbol{\Sigma}}_{n+1}} I_{\text{inc}}(\bar{\boldsymbol{F}}_{n+1}, \boldsymbol{w}_{n+1}, \Delta\lambda, \tilde{\boldsymbol{\Sigma}}_{n+1}) \big|_{\bar{\boldsymbol{F}}_{n+1}, \boldsymbol{w}_{n+1} = \text{const}}. \tag{48}$$

This staggered scheme is repeated until convergence is obtained. Finally, the macroscopic stresses can be computed from Eq. (43).

Clearly, the staggered algorithm discussed here usually does not result in an asymptotically quadratic convergence at the macroscale. One way of achieving such a behavior is the employment of a Newton-Raphson scheme at the global macroscopic level. Such an algorithm involves the algorithmic tangent

$$\bar{\mathbb{A}}_{n+1} := \frac{\mathrm{d}\bar{\boldsymbol{P}}_{n+1}}{\mathrm{d}\bar{\boldsymbol{F}}_{n+1}}. \tag{49}$$

According to Eq. (47), this tangent requires the linearization of a boundary value problem (the one defining $\boldsymbol{w}_{n+1}$). For this reason, the computation of $\bar{\mathbb{A}}_{n+1}$ is numerically very complex and often even prohibitive from a numerical point of view, cf. [5, 6].

Remark 2 *The proposed algorithm can be applied in the case of periodic or homogeneous fluctuation boundary conditions. While for homogeneous fluctuations no special consideration is needed, periodicity requires a coupling of the master and slave nodes at the facets of the RVE. Ignoring a relaxation with respect to the fluctuation field completely leads to the classical Taylor approximation.*

Remark 3 *Conceptually, the computation of the macroscopic stresses (43) is in line with standard hyperelasticity. However, the potential (42) is path-dependent and highly nonlinear. For that reason, Eq. (42) has to be solved numerically for every load step. In practice, this is done by applying the aforementioned staggered scheme, i.e., the fluctuation field is computed by solving the weak form (47) (global problem), while the update of the internal variables follows from the local minimization problem (48) (for each integration point).*

4 A novel variational hybrid homogenization method based on energy minimization

The variational homogenization method discussed in the previous section is a mathematically and from a physics point of view elegant one. However, as common to all classical FE^2 approaches, it requires the costly computation of a boundary value problem for each macroscopic material point. In this connection, the computation of the algorithmic tangent at the macroscale necessary for an asymptotically quadratic convergence is in particular very expensive. The present section is concerned with a numerically efficient approximation of the presented variational homogenization method.

4.1 Fundamentals

The mathematically, physically and numerically most desirable homogenization method is certainly the derivation of an effective, explicitly defined macroscopic constitutive model. A mathematical framework suitable for that purpose is Γ-convergence, cf. [52, 53]. Although Γ-convergence is indeed a promising technique for homogenization, its application to complex constitutive models is restricted. Nevertheless, if such an analytical solution existed, it would fulfill the Hill-Mandel condition (33) and its discrete counterpart (45). Assuming that the effective macroscopic model falls into the range of standard dissipative solids, it can be defined by a Helmholtz energy and a dissipation functional. Thus, its stress power shows the form

$$\mathcal{E}_{\text{macro}}(\dot{\bar{\boldsymbol{F}}},\dot{\bar{\mathcal{I}}}) = \dot{\Psi}_{\text{macro}}(\dot{\bar{\boldsymbol{F}}},\dot{\bar{\mathcal{I}}}) + \mathcal{D}_{\text{macro}}(\dot{\bar{\boldsymbol{F}}},\dot{\bar{\mathcal{I}}}) \tag{50}$$

with $\mathcal{I}$ being the collection of all macroscopic strain-like internal variables. In Eq. (50), the analytical solution has been marked by the subscript "macro". Consequently, if such a function existed, it would fulfill the condition

$$\bar{\mathcal{E}}_{\text{red}}(\dot{\bar{\boldsymbol{F}}}) = \inf_{\dot{\mathcal{I}}} \mathcal{E}_{\text{macro}}(\dot{\bar{\boldsymbol{F}}},\dot{\bar{\mathcal{I}}}). \tag{51}$$

As a result, combining Eq. (51) with the Hill-Mandel condition (33) yields

$$\inf_{\dot{\mathcal{I}}} \mathcal{E}_{\text{macro}}(\dot{\bar{\boldsymbol{F}}},\dot{\bar{\mathcal{I}}}) - \inf_{\dot{\boldsymbol{w}}} \inf_{\lambda,\tilde{\boldsymbol{\Sigma}}} \left\{ \frac{1}{|\mathcal{B}|} \int_{\mathcal{B}} \mathcal{E}(\dot{\bar{\boldsymbol{F}}},\dot{\boldsymbol{w}},\lambda,\tilde{\boldsymbol{\Sigma}})\, \mathrm{d}V \right\} = 0. \tag{52}$$

Interestingly, Eq. (52) introduces a natural distance

$$\mathcal{R}(\mathcal{E}_{\text{macro}}) := \left| \inf_{\dot{\mathcal{I}}} \mathcal{E}_{\text{macro}}(\dot{\bar{\boldsymbol{F}}},\dot{\bar{\mathcal{I}}}) - \inf_{\dot{\boldsymbol{w}}} \inf_{\lambda,\tilde{\boldsymbol{\Sigma}}} \left\{ \frac{1}{|\mathcal{B}|} \int_{\mathcal{B}} \mathcal{E}(\dot{\bar{\boldsymbol{F}}},\dot{\boldsymbol{w}},\lambda,\tilde{\boldsymbol{\Sigma}})\, \mathrm{d}V \right\} \right| \tag{53}$$

measuring the error between the averaged microscopic model and its effective macroscopic counterpart. Such a metric can be used in order to derive effective macroscopic models. For instance, if the space of all macroscopic models is denoted as $\mathcal{X}_{\text{model}}$, the effective macroscopic material law $\mathcal{E}^*_{\text{macro}}$ minimizes this distance, i.e.

$$\mathcal{E}^*_{\text{macro}} = \arg \inf_{\mathcal{E}_{\text{macro}} \in \mathcal{X}_{\text{model}}} \mathcal{R}(\mathcal{E}_{\text{macro}}) \qquad \forall \text{ loading paths} \tag{54}$$

and fulfills

$$\mathcal{R}(\mathcal{E}^*_{\text{macro}}) = 0 \qquad \forall \text{ loading paths.} \tag{55}$$

Although principle (54), together with the constraints (55), defines an effective macroscopic material model, this model can usually not be computed. The reasons for this are, at least, threefold. Firstly, the space of admissible loading paths is infinite-dimensional. The same also holds for the space of admissible macroscopic material models. Finally, both such spaces are highly non-linear and by no means standard.

4.2 A novel hierarchical homogenization approach – a Ritz-type approximation

The novel hierarchical homogenization approach to be elaborated in the present section is based on a Ritz-type approximation of Eq. (54). More precisely and focusing directly on the numerical implementation, the discrete counterparts of Eqs. (53) and (54)

$$\mathcal{R}_{\text{inc}}(I^{\text{macro}}_{\text{inc}}) := \left| \inf_{\Delta\mathcal{I}_{n+1}} I^{\text{macro}}_{\text{inc}}(\bar{\boldsymbol{F}}_{n+1}, \Delta\mathcal{I}_{n+1}) - \inf_{\boldsymbol{w}_{n+1}} \inf_{\Delta\lambda,\tilde{\boldsymbol{\Sigma}}_{n+1}} \left\{ \frac{1}{|\mathcal{B}|} \int_{\mathcal{B}} I_{\text{inc}}\, \mathrm{d}V \right\} \right| \tag{56}$$

and

$$I^{\text{macro}}_{\text{inc}} = \arg \inf_{I^{\text{macro}}_{\text{inc}} \in \mathcal{X}_{\text{model}}} \left\{ \sum_{i=1}^{n_{\text{loadings}}} \mathcal{R}_{\text{inc}} I^{\text{macro}}_{\text{inc}}) \right\} \tag{57}$$

are considered in the following. Eq. (56) is obtained by applying a standard time discretization to Eq. (53). Eq. (57) already contains two approximations. On the one hand, the infinite-dimensional space of admissible loading paths has been discretized by the n_{loadings} most characteristic deformation paths. On the other hand, the error $\mathcal{R}_{\text{inc}}$ is not necessarily zero as required in Eq. (55).

Eq. (57) represents still an infinite-dimensional minimization principle, since the space of admissible material models is not finite. A well-known approximation of such a minimization principle is provided by Ritz's method. Within this method, the infinite-dimensional space $\mathcal{X}_{\text{model}}$ is approximated by a finite counterpart $\mathcal{X}^h_{\text{model}}$, i.e. $\mathcal{X}^h_{\text{model}} \subset \mathcal{X}_{\text{model}}$ and $\dim \mathcal{X}^h_{\text{model}} < \infty$. With this notation, the effective macroscopic energy is computed as

$$I^{\text{macro}}_{\text{inc}} = \arg \inf_{I^{\text{macro}}_{\text{inc}} \in \mathcal{X}^h_{\text{model}}} \left\{ \sum_{i=1}^{n_{\text{loadings}}} \mathcal{R}_{\text{inc}}(I^{\text{macro}}_{\text{inc}}) \right\}. \tag{58}$$

As evident, the numerical implementation of principle (58) crucially depends on a suitable parameterization of the space $\mathcal{X}^h_{\text{model}}$. The parameterizations used in the present paper have been determined in two steps. Firstly, the mechanical response of the RVE is computed by using a classical FE^2 approach. By interpreting the results and the underlying models for the microscale, the most important features of the macroscopic response have to be identified, e.g. symmetry groups of the elastic and the plastic behavior and hardening mechanisms (isotropic, kinematic, etc.). Secondly and finally, a phenomenological model capturing most of these effects, at least qualitatively, has to be chosen, cf. Tab. 3. Its material parameters are denoted as $\boldsymbol{X}_{\text{model}}$. Using this notation, Ritz's method (58) which now reads

$$\boldsymbol{X}_{\text{model}} = \arg \inf_{\boldsymbol{X}_{\text{model}}} \left\{ \sum_{i=1}^{n_{\text{loadings}}} \mathcal{R}_{\text{inc}}(\boldsymbol{X}_{\text{model}}) \right\} \tag{59}$$

determines the best set of material parameters $\boldsymbol{X}_{\text{model}}$. Clearly, the suitable material parameters are sometimes constrained. In this case, Eq. (59) has to be replaced by a corresponding constrained optimization.

One of the most important points regarding Eq. (59) is a good approximation of $\mathcal{X}^h_{\text{model}}$ by a reasonable macroscopic model. Fortunately, the underlying variational principle provides some guidance for this. More explicitly, model 2 related to the material parameters $\boldsymbol{X}^{(2)}_{\text{model}}$ is better than model 1, if and only if

$$\inf_{\boldsymbol{X}^{(2)}_{\text{model}}} \left\{ \sum_{i=1}^{n_{\text{loadings}}} \mathcal{R}_{\text{inc}}(\boldsymbol{X}^{(2)}_{\text{model}}) \right\} \leq \inf_{\boldsymbol{X}^{(1)}_{\text{model}}} \left\{ \sum_{i=1}^{n_{\text{loadings}}} \mathcal{R}_{\text{inc}}(\boldsymbol{X}^{(1)}_{\text{model}}) \right\}. \tag{60}$$

This inequality suggests the following procedure: Starting with an initial choice represented by $\mathcal{X}^{(1)}_{\text{model}}$ and $\boldsymbol{X}^{(1)}_{\text{model}}$, a more general model 2 in the sense of $\mathcal{X}^{(2)}_{\text{model}} \supset \mathcal{X}^{(1)}_{\text{model}}$ and $\boldsymbol{X}^{(2)}_{\text{model}}$ is considered. If

$$\Delta\mathcal{R}_{\text{inc}} = \inf_{\boldsymbol{X}^{(1)}_{\text{model}}} \left\{ \sum_{i=1}^{n_{\text{loadings}}} \mathcal{R}_{\text{inc}}(\boldsymbol{X}^{(1)}_{\text{model}}) \right\} - \inf_{\boldsymbol{X}^{(2)}_{\text{model}}} \left\{ \sum_{i=1}^{n_{\text{loadings}}} \mathcal{R}_{\text{inc}}(\boldsymbol{X}^{(2)}_{\text{model}}) \right\} \geq 0 \tag{61}$$

is sufficiently large, the old macroscopic model 1 has to be replaced by model 2. In other words, the variational principle (59) provides a natural setting for error estimation. Based on this feature, the class of admissible macroscopic models can be chosen adaptively. Similar adaptive methods can be found in [54–56]. A summary of the novel hybrid variationally consistent homogenization approach is given in Tab. 3.

Remark 4 *In practice, the choice of the space χ^h_{model}, i.e., the choice of a reasonable macroscopic material model, is supported on the one hand by the microstructure of the considered representative volume element. For instance, the microstructure in Fig. 1b, together with the knowledge that both constituents are isotropic, suggests a resulting transversely isotropic macroscopic composite. On the other hand, the computation of the residual (56) requires numerical analyses of the RVE for the most relevant loading paths. Such simulations provide important information about the macroscopic mechanical response. For instance, the macroscopic iso-contours of plastic work of a solid could be computed based on which a macroscopic yield function and the hardening mechanisms could be estimated. Finally, the aforementioned criteria are further sharpened by the variational inequality (61).*

Remark 5 *Clearly, if the set of admissible material models contains the analytical solution (if it exists), the proposed hierarchical homogenization approach based on Ritz's method is not an approximation, but automatically precisely selects this analytical solution. Otherwise Ritz's method chooses the best approximation in an energetic or Hill-Mandel sense (stress power).*

1. Selection/identification of the n_{loadings} relevant loading paths either
   - by analyzing the strain paths of the macroscopic boundary value problem
   - or by using a sufficiently large space of different loading paths
2. Computation of the RVE's mechanical response for the n_{loadings} different loading paths (#computations = $n_{\text{loadings}} \times$ load steps per path) such as
   - the iso curves of equivalent plastic strain in stress space
   - the average energy of the RVE (integrated stress power), see Eq. (45)
3. Choice of a macroscopic phenomenological constitutive model based on the RVE's mechanical response, i.e., by
   - analyzing the material's symmetry due to the underlying micro-structure
   - analyzing the shape and evolution of the iso curves of equivalent plastic work
4. Homogenization / identification of the material parameters defining the macroscopic phenomenological constitutive model by the principle of energy equivalence (59)

Table 3: Summary of the hybrid variationally consistent homogenization approach based on Ritz's method

Remark 6 *It bears emphasis that the function to be minimized $\mathcal{R}_{\text{inc}}$ depends explicitly only on the macroscopic model. Accordingly, the averaged energy corresponding to the microscale, i.e.,* $\inf_{\boldsymbol{w}_{n+1}} \inf_{\Delta\lambda,\bar{\boldsymbol{\Sigma}}_{n+1}} \{1/|\mathcal{B}| \int_{\mathcal{B}} I_{\text{inc}}\, dV\}$ *in Eq. (56), has to be computed only once in a preprocessing step for each relevant loading path. For instance, 9 different local loading paths (the 9 components of the deformation gradient F_{ij}) discretized by 6 time steps are considered in the numerical examples presented in Section 5 (see Tab. 4). Accordingly, only* $6 \times 9 = 54$ *computations of the RVE are required. Based on such computations, the parameters of the macroscopic model can be identified. For this reason, minimization problem (59) leads to a numerically very efficient algorithm.*

4.3 A congruent-to-hierarchical approach

The classical FE^2 approach discussed in Subsection 3 requires, on the one hand, the computation of an additional costly boundary value problem at every macroscopic material point. On the other hand, no guess about the resulting macroscopic response is required, i.e., the method is generic in nature. By way of contrast, the approximation advocated in Subsection 4.2 yields an explicit effective macroscopic material model which is numerically very efficient. However, for that purpose, a reasonable family of macroscopic material models has to be chosen first. In this section, a compromise between the aforementioned limiting cases is briefly sketched. It represents the missing and smooth link between the classical FE^2 approach discussed in Subsection 3 and the novel hybrid homogenization method described in Subsection 4.2. The results analyzed in the following section are, however, not based on this congruent-to-hierarchical approach. Instead, the hybrid homogenization method according to Subsection 4.2 has been implemented.

The underlying idea of the congruent-to-hierarchical approach is a continuous transition from the variational multiscale approach addressed in Section 3 to the hierarchical strategy outlined in Subsection 4.2. For that purpose, both schemes are simultaneously employed in the beginning of the respective computation. To be more precise, the hierarchical algorithm introduced in Subsection 4.2 is applied to the whole previous loading history discretized by n_{history} discrete computing steps, i.e., Eq. (59) is replaced by

$$\boldsymbol{X}_{\text{model}} = \arg \inf_{\boldsymbol{X}_{\text{model}}} \left\{ \sum_{i=1}^{n_{\text{history}}} \mathcal{R}_{\text{inc}}(\boldsymbol{X}_{\text{model}}) \right\} \tag{62}$$

and the accumulated error

$$\mathcal{R}_{\text{history}} = \frac{1}{n_{\text{history}}} \left[\inf_{\boldsymbol{X}_{\text{model}}} \left\{ \sum_{i=1}^{n_{\text{history}}} \mathcal{R}_{\text{inc}}(\boldsymbol{X}_{\text{model}}) \right\} \right] \tag{63}$$

is monitored. If $\mathcal{R}_{\text{history}}$ is less than a certain threshold value, the effective macroscopic model is a

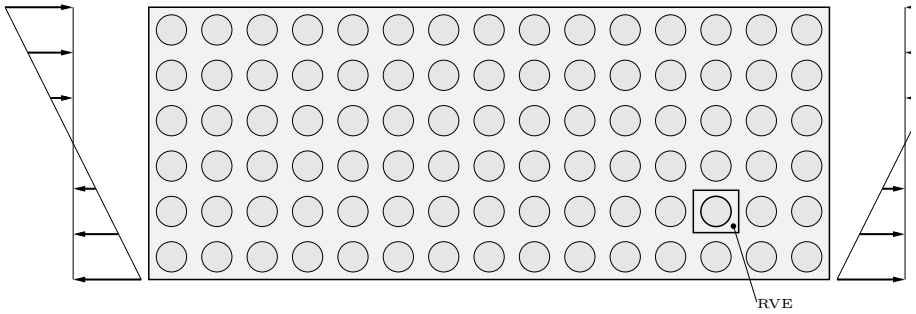

a) b)

Figure 1: Numerical analysis of a beam subjected to bending: a) geometry of the structure and boundary conditions. The dimensions of one RVE are set to 1 mm x 1 mm x 1 mm; b) triangulation of the representative volume element (RVE) showing a cylindrical inclusion

$\eta = \{-\frac{3}{120}, -\frac{2}{120}, -\frac{1}{120}, 0, +\frac{1}{120}, +\frac{2}{120}, +\frac{3}{120}\}$

Table 4: Numerical analysis of a beam subjected to bending: chosen loading history of the macroscopic deformation gradient required for the variational hierarchical multiscale approach according to Subsection 4.2 (see also Eq. (59)). The macroscopic deformation gradient is parameterized as $\bar{\boldsymbol{F}} = \boldsymbol{1} + \eta\, \boldsymbol{e}_i \otimes \boldsymbol{e}_j$ with $\boldsymbol{e}_j$ denoting the standard cartesian bases. η is varied for each loading direction independently resulting in $9 \times 6 = 54$ loading points.

reasonably good approximation of the microstructure's response. In this case, the effective macroscopic model can be used. Otherwise, the full resolution provided by the FE^2 approach is required.

Remark 7 *Since the computing time required for the algorithm presented in Subsection 4.2 is significantly less than the one associated with the FE^2 approach according to Section 3, the overall performance of the congruent-to-hierarchical approach is almost the same as that of the classical FE^2 approach.*

Remark 8 *The proposed algorithm can be modified with respect to several aspects. For instance, if $\mathcal{R}_{\text{history}} > tol$, a more realistic effective material model could be used.*

5 Numerical Examples

The applicability and performance of the novel hierarchical homogenization approach discussed in Subsection 4.2 are demonstrated by two representative numerical examples. In both cases, the geometry of the considered structure and the boundary conditions are given in Fig. 1a. The material response associated with the beam is driven by the underlying microstructure. In this connection, cylindrical inclusions are assumed, cf. Fig. 1b.

While a purely elastic response of the matrix and the inclusion is assumed in Subsection 5.1, a more complex elastoplastic behavior is considered in Subsection 5.2. In both subsections, the performance of the advocated homogenization method is compared to the results of a full field simulation. In order to avoid numerical artifacts with respect to the disretization, the same mesh is used in the full field simulation and for the novel homogenization approach. In the latter case, the material is assumed to be homogeneous within the whole structure. It is represented by the effective macroscopic material model predicted by the variational hierarchical multiscale approach.

According to Eq. (59), the application of the proposed hierarchical multiscale approach requires the choice of a characteristic family of constitutive models as well as the specification of the loading history. Concerning the latter, this history is locally defined by the series of deformation gradients according to Tab. 4. Other loading histories are certainly admissible as well, particularly if such histories are known in advance. However, it bears emphasis that the presented hierarchical multiscale approach is very fast and, thus, the number of loading paths and the number of points per loading paths are not crucial for the overall performance.

In all computations, periodic boundary conditions have been used for the fluctuation field $\boldsymbol{w}$. The objective function (59) was minimized by using different derivative-free optimization schemes such as the Nelder-Mead, the L-BFGS, the COBYLA and genetic optimization algorithms, cf. [50, 57].

	λ [N/mm^2]	κ [N/mm^2]
inclusion	26.9	32.4
matrix	269	324

Table 5: Numerical analysis of a beam subjected to bending: material parameters for the purely elastic constitutive model (64) describing the microscale

5.1 Hyperelasticity

Within the first example, the inclusion and the matrix defining the RVE in Fig. 1b are assumed as purely elastic and isotropic. To be more precise, both materials are described by the neo-Hooke-type hyperelastic stored energy

$$\Psi = \frac{1}{2}\,\mu\,\left(J^{-\frac{2}{3}}\,\boldsymbol{C}:\boldsymbol{1}-3\right)+\frac{1}{4}\,\kappa\,\left(J^2-1\right)-\frac{1}{2}\,\kappa\,\ln J \tag{64}$$

where κ and μ are the bulk modulus and the shear modulus and $J := \det \boldsymbol{F}$ is the Jacobian determinant. Hence, the material response of the RVE is determined by four material parameters. They are summarized in Tab. 5. According to Tab. 5, the inclusion is ten times weaker than the surrounding matrix material.

A suitable parameterization of the macroscopic model is needed next. Since hyperelastic models have been adopted for the RVE, the resulting effective macroscopic material law is expected to show the same reversibility of the energy. Furthermore, the geometry of the RVE in Fig. 1b suggests a transversal isotropic behavior. For this reason, a general orthotropic macroscopic constitutive framework is chosen which captures the aforementioned features. One such model is given by the Helmholtz energy

$$\begin{aligned}\bar{\Psi} = &\frac{1}{2}\,\mu\,\left(J^{-\frac{2}{3}}\,\boldsymbol{C}:\boldsymbol{1}-3\right)+\frac{1}{4}\,\kappa\,\left(J^2-1\right)-\frac{1}{2}\,\kappa\,\ln J\\ &+\frac{1}{2}\left(\alpha_1\,J_4^2+\alpha_2\,J_6^2\right)+2\left(\alpha_3\,J_5+\alpha_4\,J_7\right)\\ &+\alpha_5\,J_4\,J_1+\alpha_6\,J_6\,J_1+\alpha_7\,J_4\,J_6\end{aligned} \tag{65}$$

where $\alpha_1,\ldots,\alpha_7$ are material parameters and $J_4,\ldots,J_7$ are additional pseudo invariants, cf. [58]. They depend on the structural tensors $\boldsymbol{M}^{(i)}$ as well as on the Green-Lagrange-deformation tensor $\boldsymbol{E} := \frac{1}{2}\,(\boldsymbol{C}-\boldsymbol{1})$ and are defined as

$$\begin{aligned} J_4 &:= \boldsymbol{E}:\boldsymbol{M}^{(1)}, & J_5 &:= \boldsymbol{E}^2:\boldsymbol{M}^{(1)},\\ J_6 &:= \boldsymbol{E}:\boldsymbol{M}^{(2)}, & J_7 &:= \boldsymbol{E}^2:\boldsymbol{M}^{(2)}. \end{aligned}$$

The structural tensors $\boldsymbol{M}^{(i)}$ span the orthotropy of the material and can be written in the most general case as

$$\boldsymbol{M}^{(1)} := \boldsymbol{R}^T(\beta_1,\beta_2,\beta_3)\cdot\boldsymbol{e}_1\otimes\boldsymbol{e}_1\cdot\boldsymbol{R}(\beta_1,\beta_2,\beta_3), \tag{66}$$

$$\boldsymbol{M}^{(2)} := \boldsymbol{R}^T(\beta_1,\beta_2,\beta_3)\cdot\boldsymbol{e}_2\otimes\boldsymbol{e}_2\cdot\boldsymbol{R}(\beta_1,\beta_2,\beta_3). \tag{67}$$

In Eqs. (66) and (67), $\boldsymbol{R}$ is a rotation tensor depending on the (so far unknown) Euler angles β_i, cf. [59] and $\boldsymbol{e}_1$ and $\boldsymbol{e}_2$ define the first two cartesian bases. Combining Eq. (65) with Eqs. (66) and (67), the macroscopic material model depends on the twelve unknown parameters

$$\boldsymbol{X}_{\text{model}} = \left(\lambda,\kappa,\alpha_1,\alpha_2,\ldots\alpha_7,\beta_1,\beta_2,\beta_3\right). \tag{68}$$

These parameters have been computed by the variational Ritz's method. In this connection and according to Tab. 4, the RVE in Fig. 1b was numerically computed 54 times (9 loading paths discretized by means of 6 points each). That corresponds to Step 2 in Tab. 3. Subsequently, the variationally consistent identification of the material parameters was realized by Step 4 in Tab. 3, i.e., by minimization of Eq. (59). The best results were obtained by using the Nelder-Mead minimization algorithm. The whole optimization took less than 2 minutes on a standard PC. The final material parameters determined by the algorithm are summarized in Tab. 6. According to Tab. 6, the angle β_1 is close to zero. Speaking in terms of physics, that implies an almost transversely isotropic response which is in good agreement with the underlying microstructure.

λ [N/mm^2]	κ [N/mm^2]	α_1 [N/mm^6]	α_2 [N/mm^6]	α_3 [N/mm^6]	α_4 [N/mm^6]	α_5 [N/mm^6]	α_6 [N/mm^6]	α_7 [N/mm^6]
165.0	244.8	-15.18	-12.39	30.23	-9.403	-11.67	13.45	-45.61

β_1	β_2	β_3
$-1.379°$	$14.93°$	$18.44°$

Table 6: Numerical analysis of a beam subjected to bending – fully elastic response: material parameters defining the effective macroscopic constitutive model (see Eq. (65) and Eqs. (66) and (67))

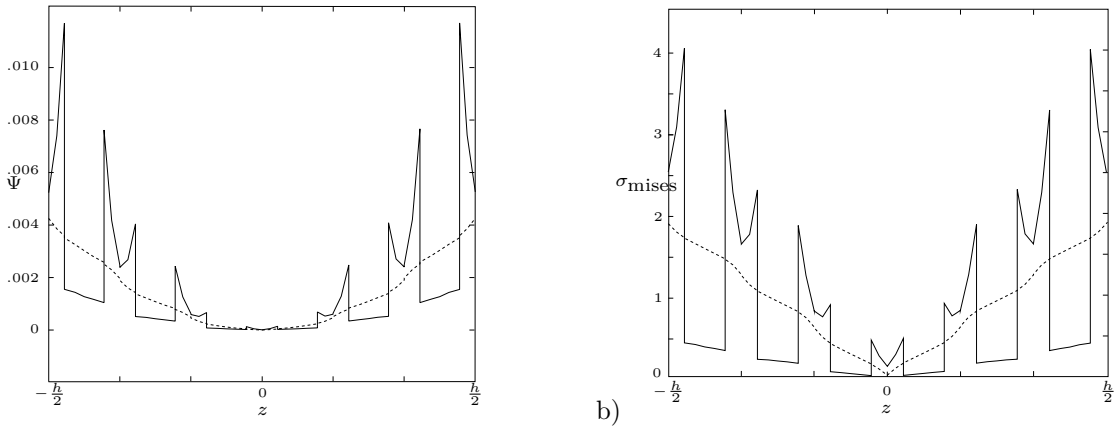

Figure 2: Numerical analysis of a beam subjected to bending – fully elastic response: a) distribution of the elastic energy Ψ along the cross-section in the middle of the beam through the inclusions; b) distribution of the equivalent von Mises stress along in the cross-section the middle of the beam through the inclusions; the solid lines correspond to the full field finite element simulation, while the dashed line is associated with the novel hybrid homogenization method

	λ [N/mm^2]	κ [N/mm^2]	Q_0^{eq} [N/mm^2]	$[\mathbb{D}]_{ijkl}$ [–]
inclusion	269	324	1.5	$\delta_{ik}\delta_{jl}$
matrix	269	324	(purely elastic)	$\delta_{ik}\delta_{jl}$

Table 7: Numerical analysis of a beam subjected to bending: material parameters for the elastoplastic constitutive model according to Eq. (64) and Eq. (69) describing the mechanical response at the microscale

Based on the effective macroscopic material model, the beam depicted in Fig. 1 is numerically analyzed. The results, together with those related to a full field simulation, are given in Fig. 2. In this figure, the distribution of the elastic energy Ψ as well as the distribution of the equivalent von Mises stress are plotted along the cross-section in the middle of the beam. Qualitatively, the plot associated with the energy and that related to the stresses look similar. In both cases, only the full field simulation can capture the interfaces between the matrix and the inclusion. However, the effective macroscopic model describes the result of the microstructure in average very well. It bears emphasis that the same holds also for classical FE^2 computations, i.e., the effect of interfaces within the RVE cannot be explicitly seen at the macroscale either. For this reason, the novel approach and the classical FE^2 method give almost identical results. However, the novel scheme is computationally significantly more efficient. For the sake of completeness, the error in the vertical displacement in the middle of the beam is reported as well. It is 0.318%.

Certainly, the results associated with the macroscopic boundary value problem depend on the material parameters of the macroscopic phenomenological constitutive model which, in turn, depend on the considered loading paths (see Tab. 4). Since the macroscopic problem is dominated by bending effects around the X_3 axis, the probably most important loading paths is defined by F_{11}. Therefore, this a priori known loading path has also been considered in the calibration procedure (among other loading paths, cf. Tab. 4). However, as mentioned in Remark 6, the proposed algorithm is numerically very efficient and thus, the number of loading paths is not critical for the overall performance. As a consequence, a broad spectrum of different loading paths should be employed, if no information concerning the relevant loading state is known in advance.

5.2 Elastoplasticity

Next, the numerical example is reanalyzed assuming a more complex constitutive model at the microscale. Since the previous section was exclusively concerned with elasticity, focus here is on the elastoplastic response. For this reason, the elastic properties are assumed as homogeneously distributed, i.e., the same material parameters are chosen for the matrix and the inclusion, see Fig. 1b. Consequently, the same behavior is also considered for the macroscale. Concerning plasticity, the isotropic von Mises type yield function

$$\phi = \sqrt{\operatorname{dev}\boldsymbol{\Sigma} : \operatorname{dev}\boldsymbol{\Sigma}} - Q_0. \tag{69}$$

is employed in order to describe the microscale. Here, $\operatorname{dev}\boldsymbol{\Sigma}$ is the deviatoric part of the stresses and Q_0 denotes the yield stress.

In order to choose a reasonable family of macroscopic models capturing the features of the microscale, Eq. (69) is combined with the underlying microstructure, cf. Step 2 in Tab. 3. That leads to a purely deviatoric yield function showing transversal isotropy at the macroscale. Accordingly, the Hill-type class of yield functions

$$\bar{\phi} = \sqrt{\bar{\boldsymbol{\Sigma}} : \mathbb{H} : \bar{\boldsymbol{\Sigma}}} - \bar{Q}_0^{\mathrm{eq}} \tag{70}$$

is adopted. The 4th-order weighting tensor $\mathbb{H}$ is decomposed into a deviatoric projection $[\mathbb{P}^{\mathrm{dev}}]_{ijkl} := \delta_{ik}\delta_{jl} - \frac{1}{3}\,\delta_{ij}\delta_{kl}$ and an additional tensor $\mathbb{D}$ corresponding to the symmetry of the material, i.e.

$$\mathbb{H} = \mathbb{P}^{\mathrm{dev}} : \mathbb{D} : \mathbb{P}^{\mathrm{dev}}. \tag{71}$$

Clearly, if $[\mathbb{D}]_{ijkl} = \delta_{ik}\delta_{jl}$, Eq. (70) yields the classical von Mises yield function.

For the sake of simplicity, perfect plasticity is considered. However, complex hardening models can be included in the proposed variational multiscale approach in a straightforward manner. The only requirement is the variational consistency of the models, cf. [20, 21, 60].

$\mathbb{D}_{1111}$	$\mathbb{D}_{1212}$	$\mathbb{D}_{1313}$	$\mathbb{D}_{2121}$	$\mathbb{D}_{2222}$	$\mathbb{D}_{2323}$	$\mathbb{D}_{3131}$	$\mathbb{D}_{3232}$	$\mathbb{D}_{3333}$
1.056	0.9907	0.9786	1.010	0.9994	0.9893	1.014	1.000	1.021

Table 8: Numerical analysis of a beam subjected to bending – elastoplastic response: dimensionless material parameters defining the effective macroscopic constitutive model

According to Eq. (70), the material parameters

$$\boldsymbol{X}_{\text{model}} = (\mathbb{D}, Q_0) \tag{72}$$

have to be computed for the effective macroscopic material model. Eq. (72) yields an 82-dimensional approximation of the space of admissible macroscopic models. However, that space is not unconstrained. For instance, the yield function is usually assumed to be convex. Unfortunately, the respective constraint is highly non-linear and thus difficult to enforce. For this reason, the matrix representing the tensor $\mathbb{D}$ is assumed to show a diagonal form (in Voigt notation). On the one hand, that complies with the expected orthotropy (transversal isotropy) of the effective macroscopic yield function. On the other hand, convexity in this case simply requires that the eigenvalues of $\mathbb{D}$ are greater than zero. This choice reduces the number of unknowns from 82 to 10. It bears emphasis that the initial diameter of the yield function can either be defined by Q_0 or by the 4th-order tensor $\mathbb{D}$. Consequently, the admissible choice $Q_0 = 1.5$ N/ mm^2 has been made. In summary, the 9-dimensional reduced set of unknown material parameters is thus

$$\boldsymbol{X}_{\text{model}} = (\mathbb{D}_{1111}, \mathbb{D}_{1212}, \mathbb{D}_{1313}, \mathbb{D}_{2121}, \mathbb{D}_{2222}, \mathbb{D}_{2323}, \mathbb{D}_{3131}, \mathbb{D}_{3232}, \mathbb{D}_{3333}). \tag{73}$$

The macroscopic material parameters (73) were again computed by means of the novel hybrid homogenization method discussed in Subsection 4.2. In line with the previous subsection, the variational material parameter identification procedure requires the selection of the n_{loadings} relevant loading paths, see Step 1 in Tab 3. Following the previous section, the different components of the deformation gradient are varied independently for that purpose, see Tab. 4. In contrast to the hyperelastic model considered in the previous section, plasticity is intrinsically a path-dependent process. For this reason, the order of the different loading paths matters. In the computations, a virgin material without plastic deformation was considered for each of the 9 different loading paths (defined by the components Fij). Clearly, the increase in plastic deformation within each of the 9 loading steps was taken into account. The assumption of resetting the plastic deformation history for each of the 9 different loading steps is related to the assumption of radial or proportional loading paths, i.e., in case of strong loading path changes within the macroscopic boundary value problem, this assumption is not valid. However, depending on the considered example, loading in 11 direction followed directly by loading in 22 direction without unloading could also be implemented. Consequently, the proposed algorithm is general enough to deal also with such more complicated loading paths. In summary, the elasto-plastic RVE shown in Fig. 1b is numerically computed for 9 independent load paths (defined by the components Fij). Each of them is discretized by 6 time steps, cf. Tab. 4. Consequently, $9 \times 6 = 54$ computations of the RVE are required (see Step 2 in Tab. 3). Subsequently, a homogeneous RVE modeled by means of the macroscopic model is also numerically analyzed for the same 54 load steps. These 54 computations, depending on the involved model parameters of the macroscopic model, are repeated for different parameters until Eq. (59) is minimized. For this reason, the minimization is not performed for one single time step, but for the whole loading history. By doing so, the path-dependence of the process is naturally included. In contrast to the previous example, the best results were obtained by applying a genetic algorithm to the optimization problem (59). The material parameters corresponding to the final state are summarized in Tab. 8.

Based on the material parameters in Tab. 8, the beam depicted in Figs. 1a and 1b was reanalyzed. Following the hyperelastic case, a full field finite element simulation is additionally considered for the sake of comparison. The predicted distribution of the integrated stress power $\bar{I}_{\text{inc}}$, as well as that of the equivalent von Mises stress along the cross-section in the middle of the beam are given in Fig. 3. From these figures it can be seen that the effective material model indeed captures the mechanical response induced by the underlying microstructure very well. Only if a higher resolution concerning the material interfaces is required, the effective macroscopic material model relying on an averaging scheme will not be sufficient any more. However, a classical FE^2 approach would not be sufficient either then.

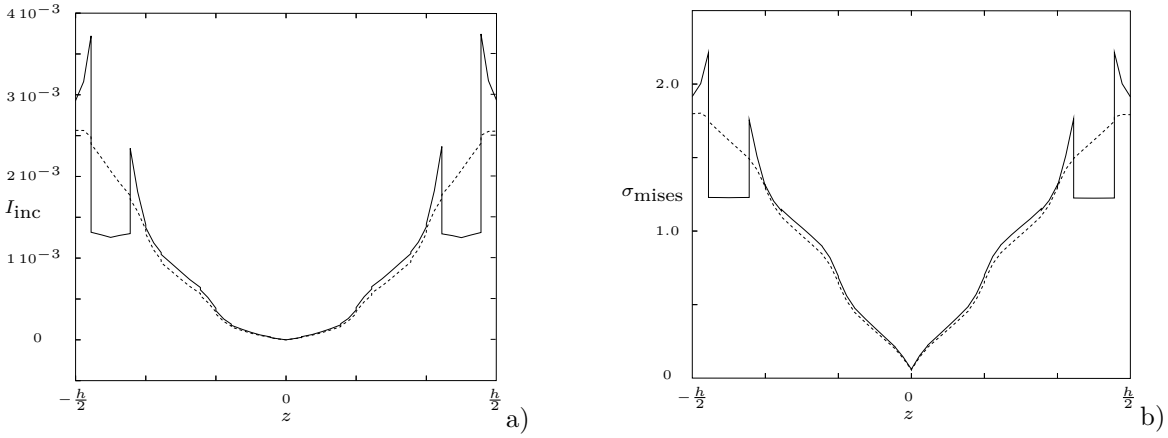

Figure 3: Numerical analysis of a beam subjected to bending – elastoplastic response: a) distribution of the integrated stress power $\bar{I}_{\text{inc}}$ along the cross-section in the middle of the beam through the inclusions; b) distribution of the equivalent von Mises stress along in the cross-section the middle of the beam through the inclusions; the solid lines correspond to the full field finite element simulation, while the dashed line is associated with the novel hybrid homogenization method

6 Conclusions

A novel hybrid homogenization method was proposed in the present paper. The backbone of this approach is a variationally consistent description of the constitutive models for the microscale as well as for the macroscale. This description defines all state variables naturally as energy minimizers of an incrementally defined energy potential. Furthermore, it suggests the canonical principle of energy equivalence for coupling the different scales. Since a classical FE^2 approach of this variationally consistent scale bridging is numerically very extensive, an efficient approximation was advocated. This approximation crucially depends on the overriding minimization principle governing every aspect of the multiscale problem. To be more precise, Ritz's method was used as an approximation. By doing so, the material parameters defining an effective macroscopic material model capturing the underlying microstructure could be efficiently computed. The only difficulty related to the presented algorithm is the choice of a suitable material model describing all relevant features of the microscale. However, the variational scale bridging principle provides some guidance for this. To be more explicit, model 2 is better than model 1 if, and only if, the respective energy is lower. Comparisons between the results predicted by the novel hybrid homogenization method and full field finite element simulations clearly showed that the novel method is indeed very promising.

Acknowledgement

Financial support from the German Research Foundation (DFG) via SFB 986 (M^3), project A5, is gratefully acknowledged.

References

[1] H. P. Feigenbaum and Y. F. Dafalias. Directional distortional hardening in metal plasticity within thermodynamics. *Int. J. Solids Struct.*, 44:7526–7542, 2007.

[2] S. Nemat-Nasser and M. Hori. *Micromechanics: Overall properties of heterogeneous materials.* Elsevier, 1999.

[3] S. Li and G. Wang. *Micromechanics and Nanomechanics.* World Scientific, 2008.

[4] T.I. Zhodi and P. Wriggers. *Introduction to Computational Micromechanics.* Springer, Berlin, 2005.

[5] C. Miehe. Strain-driven homogenization of inelastic microstructures and composites based on an incremental variational formulation. *International Journal for Numerical Methods in Engineering*, 55:1285–1322, 2002.

[6] C. Miehe, J. Schotte, and M. Lambrecht. Homogenization of inelastic solid materials at finite strains based on incremental minimization principles. application to the texture analysis of polycrystals. *Journal of the Mechanics and Physics of Solids*, 50(10):2123–2167, 2002.

[7] Z. Yuan and J. Fish. Toward realization of computational homogenization in practice. *International Journal for Numerical Methods in Engineering*, 73(3):361–380, 2008.

[8] J.D. Eshelby. The determination of the elastic field of an ellipsoidal inclusion. *Proceedings of the Royal Society A*, 241:376–396, 1957.

[9] J.D. Eshelby. The elastic field outside an ellipsoidal inclusion. *Proceedings of the Royal Society*, 252:561–569, 1959.

[10] B. Budiansky. On the elastic moduli of some heterogeneous materials. *Journal of the Mechanics and Physics of Solids*, 13:223–227, 1965.

[11] R. Hill. A self-consistent mechanics of elastoplastic polycrystals. *Journal of the Mechanics and Physics of Solids*, 13:213–222, 1965.

[12] K. Tanaka and T. Mori. Note on volume integrals of the elastic field around an ellipsoidal inclusion. *Journal of Elasticity*, 2:199–200, 1972.

[13] R.A. Lebensohn and C.N. Tome. A selfconsistent approach for the simulation of plastic deformation and texture development of polycrystals: application to zirconium alloys. *Acta Metallurgica et Materialia*, 41:2611–2624, 1993.

[14] P.M. Suquet. Local and global aspects in the mathematical theory of plasticity. In A. Sawczuck and G. Bianchi, editors, *Plasticity Today: Modelling, Methods and Applications*, pages 279–310. Elsevier Applied Science Publishers, London, 1985.

[15] J. Guedes and N. Kikuchi. Preprocessing and postprocessing for materials based on the homogenization method with adaptive finite element methods. *Computer Methods in Applied Mechanics and Engineering*, 83(2):143–198, 1990.

[16] J. Michel and P. Suquet. Nonuniform transformation field analysis. *International Journal of Solids and Structures*, 40:6937–6955, 2003.

[17] M. Ortiz and L. Stainier. The variational formulation of viscoplastic constitutive updates. *Computer Methods in Applied Mechanics and Engineering*, 171:419–444, 1999.

[18] C. Carstensen, K. Hackl, and A. Mielke. Non-convex potentials and microstructures in finite-strain plasticity. *Proc. R. Soc. Lond. A*, 458:299—-317, 2002.

[19] H. Petryk. Incremental energy minimization in dissipative solids. *Comptes Rendus Mecanique*, 331(7):469–474, 2003.

[20] J. Mosler and O.T. Bruhns. On the implementation of rate-independent standard dissipative solids at finite strain – variational constitutive updates. *Computer Methods in Applied Mechanics and Engineering*, 9–12:417–429, 2009.

[21] J. Mosler and O.T. Bruhns. Towards variational constitutive updates for non-associative plasticity models at finite strain: models based on a volumetric-deviatoric split. *International Journal of Solids and Structures*, 46:1676–1684, 2009.

[22] N. Bleier and J. Mosler. Efficient variational constitutive updates by means of a novel parameterization of the flow rule. *International Journal for Numerical Methods in Engineering*, 2011. in press.

[23] L. Brassart, L. Stainier, I. Doghri, and L. Delannay. A variational formulation for the incremental homogenization of elasto-plastic composites. *Journal of the Mechanics and Physics of Solids*, 59(12):2455–2475, 2011.

[24] S. Graff, W. Brocks, and D. Steglich. Yielding of magnesium: From single crystal to polycrystalline aggregates. *International Journal of Plasticity*, 23(12):1957–1978, 2007.

[25] B. Plunkett, R.A. Lebensohn, O. Cazacu, and F. Barlat. Anisotropic yield function of hexagonal materials taking into account texture development and anisotropic hardening. *Acta Materialia*, 54(16):4159–4169, 2006.

[26] I. Scheider. Derivation of separation laws for cohesive models in the course of ductile fracture. *Engineering Fracture Mechanics*, 76(10):1450–1459, 2009.

[27] R. W. Ogden, G. Saccomandi, and I. Sgura. Fitting hyperelastic models to experimental data. *Computational Mechanics*, 34:484–502, 2004.

[28] S. Avril, M. Bonnet, A.-S. Bretelle, M. Grediac, F. Hild, P. Ienny, F. Latourte, D. Lemosse, S. Pagano, E. Pagnacco, and F. Pierron. Overview of identification methods of mechanical parameters based on full-field measurements. *Experimental Mechanics M.*, 48(4):381–402, 2008.

[29] B. Halphen and Q.S. Nguyen. Sur les matériaux standards généralisés. *J. Méchanique*, 14:39–63, 1975.

[30] J. Mosler. Variationally consistent modeling of finite strain plasticity theory with non-linear kinematic hardening. *Computer Methods in Applied Mechanics and Engineering*, 199:2753–2764, 2010.

[31] J. Mandel. *Plasticité Classique et Viscoplasticité*. Cours and Lectures au CISM No. 97. International Center for Mechanical Sciences, Springer-Verlag, New York, 1972.

[32] J. Lemaitre. A continuous damage mechanics model for ductile fracture. *J. Eng. Mat. Techn.*, 107:83–89, 1985.

[33] M. Homayonifar and J. Mosler. On the coupling of plastic slip and deformation-induced twinning in magnesium: A variationally consistent approach based on energy minimization. *International Journal of Plasticity*, 27:983–1003, 2011.

[34] M. Homayonifar and J. Mosler. Efficient modeling of microstructure evolution in magnesium by energy minimization. *International Journal of Plasticity*, 2011. in press, DOI: 10.1016/j.ijplas.2011.05.011.

[35] Q. Yang, L. Stainier, and M. Ortiz. A variational formulation of the coupled thermo-mechanical boundary-value problem for general dissipative solids. *Journal of the Mechanics and Physics of Solids*, 54:401–424, 2006.

[36] M. Canadija and J. Mosler. On the thermomechanical coupling in finite strain plasticity theory with non-linear kinematic hardening by means of incremental energy minimization. *International Journal of Solids and Structures*, 48:1120–1129, 2011.

[37] M. Ortiz and E. A. Repetto. Nonconvex energy minimization and dislocation structures in ductile single crystals. *Journal of the Mechanics and Physics of Solids*, 47:397–462, 1999.

[38] S. Aubry, M. Fago, and M. Ortiz. A constrained sequential-lamination algorithm for the simulation of sub-grid microstructure in martensitic materials. *Computer Methods in Applied Mechanics and Engineering*, 192:2823–2843, 2003.

[39] B. L. Hansen, C. A. Bronkhorst, and M. Ortiz. Dislocation subgrain structure and modeling the plastic hardening of metallic single crystals. *Modelling and Simulation in Materials Science and Engineering*, 18:1–42, 2010.

[40] C. Miehe, F. Welschinger, and M. Hofacker. Thermodynamically consistent phase-field models of fracture: Variational principles and multi-field FE implementations. *International Journal for Numerical Methods in Engineering*, 83(10):1273–1311, 2010.

[41] C. Miehe. A multi-field incremental variational framework for gradient-extended standard dissipative solids. *Journal of the Mechanics and Physics of Solids*, 59(4):898–923, 2011.

[42] E. H. Lee and D. T. Liu. Finite strain elastic-plastic theory with application to plane-wave analysis. *Applied Physics*, 38:19–27, 1967.

[43] E. H. Lee. Elastic-plastic deformations at finite strains. *ASME, Journal of Applied Mechanics*, 36:1–6, 1969.

[44] V. Kouznetsova, M. G. D. Geers, and W. A. M. Brekelmans. Multi-scale constitutive modelling of heterogeneous materials with a gradient-enhanced computational homogenization scheme. *International Journal for Numerical Methods in Engineering*, 54(8):1235–1260, 2002.

[45] R. Hill. On constitutive macro-variables for heterogeneous solids at finite strain. *Proceedings of the Royal Society*, 326:131–147, 1972.

[46] R. Hill. Elastic properties of reinforced solids: Some theoretical principles. *Journal of the Mechanics and Physics of Solids*, 11:357–372, 1963.

[47] S. Müller. Homogenization of non convex integral functionals and cellular elastic materials. *Archive for Rational Mechanics and Analysis*, 99:189–212, 1987.

[48] J.C. Simo and T.J.R. Hughes. *Computational Inelasticity*. Springer, New York, 1998.

[49] J.C. Simo. Numerical analysis of classical plasticity. In P.G. Ciarlet and J.J. Lions, editors, *Handbook for numerical analysis*, volume IV. Elsevier, Amsterdam, 1998.

[50] C. Geiger and C. Kanzow. *Numerische Verfahren zur Lösung unrestringierter Optimierungsaufgaben*. Springer, New York, 1999.

[51] C. Geiger and C. Kanzow. *Theorie und Numerik restringierter Optimierungsaufgaben*. Springer, New York, 2002.

[52] G. Dal Maso. *An introduction to* Γ*-convergence*. Birkhäuser, Boston, 1983.

[53] A. Braides. *Gamma-convergence for Beginners*. Oxford University Press, 2002.

[54] J. Mosler and M. Ortiz. On the numerical implementation of variational arbitrary Lagrangian-Eulerian (VALE) formulations. *International Journal for Numerical Methods in Engineering*, 67:1272–1289, 2006.

[55] J. Mosler and M. Ortiz. Variational h-adaption in finite deformation elasticity and plasticity. *International Journal for Numerical Methods in Engineering*, 72:505–523, 2007.

[56] J. Mosler and M. Ortiz. An error-estimate-free and remapping-free variational mesh refinement and coarsening method for dissipative solids at finite strains. *International Journal for Numerical Methods in Engineering*, 77:437–450, 2009.

[57] J. Nocedal and S.J. Wright. *Numerical Optimization*. Springer, New York, 1999.

[58] J. Löblein. *Ein Modell zur Beschreibung finiter anisotroper elasto-plastischer Deformationen unter Berücksichtigung diskreter Rissausbreitung*. PhD thesis, Universität Duisburg-Essen, 2004.

[59] I.N. Bronstein, I. Semendjajev, G. Musiol, and H. Mühlig. *Handbook of Mathematics*. Springer, 2006.

[60] J. Mosler. Variationally consistent modeling of finite strain plasticity theory with non-linear kinematic hardening. *Computer Methods in Applied Mechanics and Engineering*, 200:3127–3138, 2010.